Topology identifies emerging adaptive mutations in SARS-CoV-2

Michael Bleher[2†*], Lukas Hahn[2†*], Juan Ángel Patiño-Galindo[3], Mathieu Carrière[4], Ulrich Bauer[5], Raúl Rabadán[3], Andreas Ott[1,2†*]

[1]Mathematics Department, Karlsruhe Institute of Technology, Karlsruhe, Germany
[2]Mathematical Institute, Heidelberg University, Heidelberg, Germany
[3]Program for Mathematical Genomics, Department of Systems Biology, Columbia University, New York, NY, USA
[4]DataShape, Inria Sophia-Antipolis, Biot, France
[5]Mathematics Department, Technical University of Munich, Munich, Germany

[†]These three authors contributed equally to this work.
[*]Correspondence: mbleher@mathi.uni-heidelberg.de
lhahn@mathi.uni-heidelberg.de
andreas.ott@kit.edu

Abstract

The COVID-19 pandemic has lead to a worldwide effort to characterize its evolution through the mapping of mutations in the genome of the coronavirus SARS-CoV-2. As the virus spreads and evolves it acquires new mutations that could have important public health consequences, including higher transmissibility, morbidity, mortality, and immune evasion, among others. Ideally, we would like to quickly identify new mutations that could confer adaptive advantages to the evolving virus by leveraging the large number of SARS-CoV-2 genomes. One way of identifying adaptive mutations is by looking at convergent mutations, mutations in the same genomic position that occur independently. The large number of currently available genomes, more than a million at this moment, however precludes the efficient use of phylogeny-based techniques. Here, we establish a fast and scalable Topological Data Analysis approach for the early warning and surveillance of emerging adaptive mutations of the coronavirus SARS-CoV-2 in the ongoing COVID-19 pandemic. Our method relies on a novel topological tool for the analysis of viral genome datasets based on persistent homology. It systematically identifies convergent events in viral evolution merely by their topological footprint and thus overcomes limitations of current phylogenetic inference techniques. This allows for an unbiased and rapid analysis of large viral datasets. We introduce a new topological measure for convergent evolution and apply it to the complete GISAID dataset as of February 2021, comprising 303,651 high-quality SARS-CoV-2 isolates taken from patients all over the world since the beginning of the pandemic. A complete list of mutations showing topological signals of convergence is compiled. We find that topologically salient mutations on the receptor-binding domain appear in several variants of concern and are linked with an increase in infectivity and immune escape. Moreover, for many adaptive mutations the topological signal precedes an increase in prevalence. We demonstrate the capability of our method to effectively identify emerging adaptive mutations at an early stage. By localizing topological signals in the dataset, we are able to extract geo-temporal information about the early occurrence of emerging adaptive mutations. The identification of these mutations can help to develop an alert system to monitor mutations of concern and guide experimentalists to focus the study of specific circulating variants.

Introduction

The COVID-19 pandemic has led to millions of lost human lives and devastating economic impact worldwide. The pandemic was caused by a coronavirus, SARS-CoV-2, likely to have originated from an animal reservoir [1, 22, 29, 32]. As the virus has spread through the world, it has been mutating and acquiring new mutations in its genome. Although most of the mutations could be deleterious or neutral, a few of them could be advantageous for the virus, for instance, by increasing its infectivity or by helping it to avoid the immune system. As more people develop immune protection by previous viral infections or through vaccination, it is important to rapidly and effectively identify mutations that could confer the virus some adaptive advantage.

One approach to identify potential adaptive mutations is by experimentally mutating many positions and testing the effect of these mutations in certain phenotypes, like binding to the human receptor or immune escape [9, 35, 45]. However, the number of mutations in the viral genome is extraordinarily large and this number is even larger when different genetic backgrounds are considered. Experimental approaches are limited by the vast number of potential variations.

Another approach to identify adaptive mutations, that relies only on the genomic information of the virus, is to look for mutations in a particular genomic locus that occurs multiple times, more than what one expected. If a mutation is deleterious, we should not be able to observe it frequently and when observed, its presence should not increase in frequency as time goes by. However, if a mutation gives some sort of advantage to the virus, we should expect that it could occur in several places independently and that its frequency should increase with time. We have several examples of these kind of mutations already observed in the COVID-19 pandemic. For instance, the D614G mutation in the Spike gene was early identified in the pandemic and is now found in most of the virus isolates [21].

The genomic-based approaches to identify adaptive mutations also have the advantage that there is a worldwide effort to sequence viruses with currently more than a million genomes available to the scientific community. As the pandemic evolves, the technology becomes more accessible, and the public health and political will to characterize variants increases, we should expect this number to grow, leading to an almost real-time genomic data acquisition for the real-time surveillance of concerning variants. Ideally, we would like to have a method that will leverage all genomic information at real-time to rapidly inform public health authorities about the emergence of potential mutations of concern [14].

The most standard way to identify these adaptive mutations is based on the aforementioned idea that mutations that confer an adaptive advantage occur repeatedly in the population and increase in frequency. For this analysis one needs to construct a phylogenetic tree of the genomes available and identify mutations that occur in independent branches. That is the idea behind software packages like TreeTime and HomoplasyFinder [5, 34]. HomoplasyFinder has been used to study convergent evolution in SARS-CoV-2 during earlier phases of the pandemic [39, 40]. Phylogenetic approaches, however, become daunting as the number of sequences increases, and become a major challenge when the number of genomes exceeds the tens of thousands. That is due to the scaling of the number of potential phylogenetic trees with the number of genomes. Although there are approximations based on subsamples of sequences adapted to the focus of the analysis, like for example in Nextstrain [12], these methods rarely scale to the numbers of SARS-CoV-2 genomes currently available. In addition to the complexity due to the large number of sequences, the phenomenon that we are interested in characterizing, the independent emergence of mutations, gives rise to homoplasies that confuse the generation of phylogenetic trees. This leads to the necessity of masking problematic sites that induce instabilities in the inferred phylogenies [38]. Furthermore, it has been observed that in producing a single optimal phylogeny for SARS-CoV-2 one generally faces serious difficulties, as the number of

sequences is large while the genetic diversity is low [28]. Ideally, we would like a method that identifies potential adaptive mutations without the need of constructing a phylogenetic tree.

Here we propose a method based on Topological Data Analysis (TDA) that can efficiently identify convergent mutations without the need to construct a phylogenetic tree and that can easily scale to hundreds of thousands of genomes. We show how this method can identify known and potentially relevant new adaptive mutations even at low frequencies in the populations.

Results

Topological Data Analysis and viral evolution. Chan et al. [3] proposed a method from Topological Data Analysis known as persistent homology[1] to extract global features from genomic datasets that capture evolutionary processes that can be represented by a tree (vertical) or a network (reticulate) at various scales of genetic distance. In this approach, in place of a single phylogenetic tree or network, the core structure is a sequence of objects, one for each dimension, which incorporates many potential evolutionary relationships between the corresponding isolates in a comprehensive and efficient way. While persistent homology in dimension zero reproduces aspects of vertical evolution in terms of hierarchical clustering, it has been established that the presence of persistent homology above dimension zero necessarily implies that the corresponding evolutionary history cannot be fully

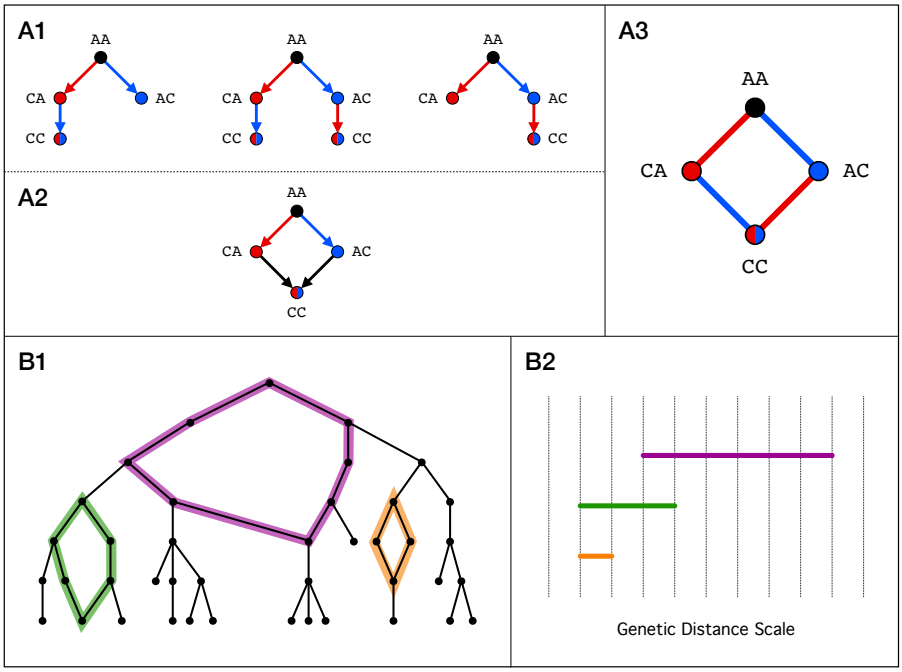

Figure 1. Topological Data Analysis detects reticulate events in viral evolution. (A) Reticulate events in molecular evolution create topological cycles. (A1) and (A2) show possible evolutionary histories on the level of individuals in the example of a genome with only two nucleotides. The coloring of the edges corresponds to the acquisition of a specific mutation, while the coloring of the nodes represents individuals carrying this mutation. Convergent evolution (A1) or recombination (A2) leads to the presence of four alleles for which there is no single consistent phylogeny (four-gamete test). On the genomic level, identical individuals cannot be distinguished and incompatible phylogenies are represented by a topological cycle in the corresponding phylogenetic network (A3). (B) Persistent homology in dimension one detects reticulate events in viral evolution by means of a persistence barcode. Each bar in the barcode (B2) corresponds to a topological cycle in the reticulate phylogeny (B1). Bars starting at higher genetic distance scale correspond to cycles with edges of longer genetic distance. The length of a bar indicates the size of the corresponding cycle.

[1]Throughout this paper, the term *homology* refers to the notion from the mathematical field of topology.

explained by a single phylogenetic tree. The mathematical background of this phenomenon is a classical theorem due to Rips, which asserts that trees have trivial persistent Vietoris-Rips homology [11]. In particular, persistent homology in dimension one detects topological cycles in the genomic dataset, in which case phylogenetic reconstruction methods can produce ambiguous tree topologies. Figure 1 shows the simplest examples of such inconsistencies and how they can be represented in terms of a reticulate phylogeny. For a given sequence alignment, persistent homology extracts its inherent topological patterns and compiles it to a stable and unbiased descriptor known as a *persistence barcode*. Each bar in the barcode corresponds to a topological cycle in the associated reticulate phylogeny, which can be traced back to the explicit isolates that comprise the reticulate event (Figure 1).

There are several scenarios that can lead to reticulate events. For instance, if a genome of an organism imports genetic material from a different genome, in lateral gene transfer for instance, we will observe that parts of the newly generated genome resemble the parent, while others resemble the genome of the organism that exported that material. Recombination and reassortments are common phenomena observed in viruses where two parental strains co-infect the same host cell generating a new virus containing genetic material from both parental strains. But similarity between genomes can also be generated at smaller scales, when the same mutation occurs independently twice, making the two strains more similar than expected. Persistent homology captures all these events, and also the scale of the events. Although in general it requires care to infer the biological origin of a given topological cycle, in viral evolution one expects bars at small scales to correspond mostly to homoplasies, while well-supported recombination signals typically produce topological features at larger scales, as entire blocks of genetic material are exchanged in the process.

Quantification of topologically recurrent mutations. In order to identify signals of convergent evolution in SARS-CoV-2, we define a novel index of recurrence in reticulate phylogenies that is based on persistent homology and does not rely on a possibly sub-optimal tree reconstruction. We use a specifically designed algorithm, implemented in a recent version of `Ripser` [2], that associates to each bar in the persistence barcode an explicit topological cycle given by a series of isolates that approximates all potentially relevant evolutionary steps as faithfully as possible (see Methods). We further consider only *SNV cycles*, for which adjacent sequences only differ by single nucleotide variations (SNV) and that do not include more than one substition per site (Figure 2). In the barcode, these cycles are associated to bars that start at genetic distance scale 1. The *topological recurrence index (tRI)* of a specific mutation is then the total number of SNV cycles in the reticulate phylogeny that contain this

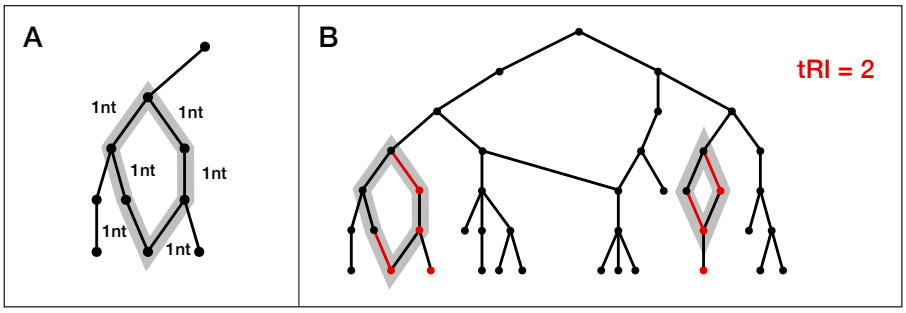

Figure 2. The topological recurrence index (tRI) quantifies convergent evolution. (A) SNV cycles are formed by single nucleotide variations only. All virus isolates in the cycle have genetic distance one. Without multiple substitutions per site, the fact that a topological cycle closes up necessarily implies that all SNVs in this cycle appear twice, independently of each other and distributed across both possible lineages. (B) The topological recurrence index (tRI) is the total number of SNV cycles in the phylogeny that contain a specific SNV. In the example shown, the red SNV is contained in two distinct cycles and therefore has a tRI of 2. The tRI gives a lower bound for the number of independent occurrences of a given mutation during the evolution of the virus.

mutation (Figure 2). The tRI provides a lower bound for the number of independent occurrences of a given mutation during the evolution of the virus. It is therefore a measure for convergent evolution.

Persistent homology of the GISAID dataset. To characterize the extent to which reticulate events shape the evolution of SARS-CoV-2, we computed the persistence barcode of a curated alignment of 161,024 genetically distinct viral genomes from human and animal hosts representing the evolution of the pandemic since its beginning in late 2019. The alignment was compiled from all 303,651 high quality genomes in the complete GISAID EpiCoV dataset as of 28 February 2021. The computation involved the generation of a genetic distance matrix (Hamming distance) of the dataset with `Hammingdist` [20] and the subsequent computation of its persistence barcode with `Ripser` [2] (see Methods). The resulting barcode is shown in Figure 3 and features 2,899 bars across all genetic distance scales at the current level of diversification. Each bar in the barcode corresponds to a one-dimensional topological cycle in the dataset and indicates the presence of a reticulate event in the evolutionary history of the virus. For RNA viruses like SARS-CoV-2, possible biological mechanisms underlying reticulate evolution include homologous recombinations and homoplasies through convergent evolution. Notably, the vast majority of topological features in the GISAID dataset is concentrated at small genetic distance scales and is expected to be associated mainly to homoplasic sites. In large genomic datasets, homoplasies can arise randomly, which leads to a certain amount of statistical noise in the persistence barcode. Another important source of topological features are systematic sequencing inaccuracies, either through contamination of the sequenced isolates or acquisition of an improper consensus genome [24, 25]. Here, we present a careful investigation of the topological features of the GISAID dataset at small scales and develop a pipeline that allows us to separate statistical noise from real biological signals for convergence.

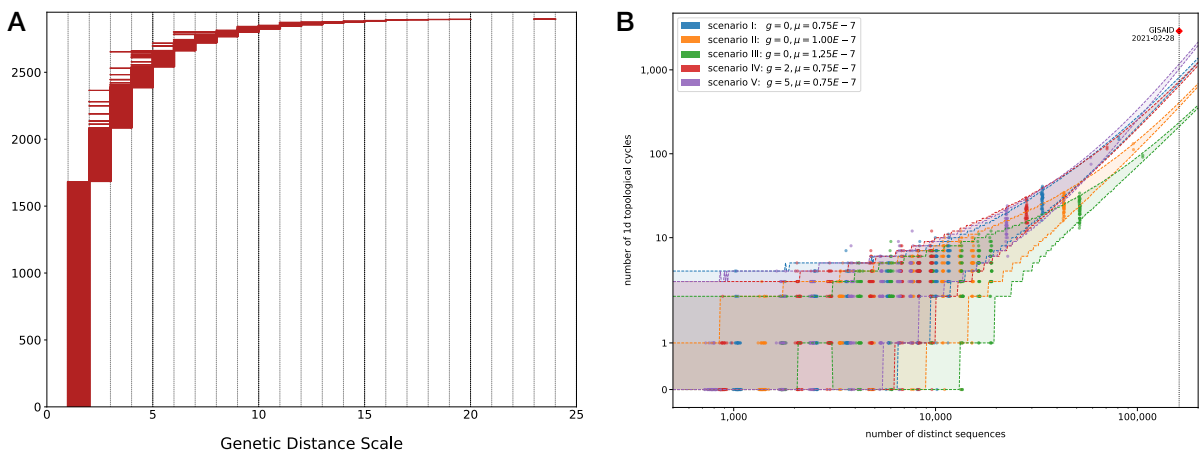

Figure 3. Topological Data Analysis of the GISAID dataset and simulated viral evolution. (A) Persistence barcode representing the persistent homology in dimension one of the complete GISAID dataset as of February 2021, containing 161,024 genetically distinct high-quality SARS-CoV-2 genomes and representing the evolution of the pandemic since its beginning in late 2019 (see Methods). Each of the 2,899 bars in the barcode corresponds to a topological cycle in the reticulate phylogeny. The rich topology of the dataset indicates a multitude of reticulate events that shaped the evolution of the virus in the course of the pandemic. (B) Topological features are satistically significant. Simulations were generated with SANTA-SIM [19] for five distinct scenarios with varying growth rate g and mutation rate μ (see Table 1). The 95% prediction intervals for the number of one-dimensional cycles in each scenario are based on the extrapolation of a Panjer distribution for an increasing number of distinct sequences in the simulated phylogenies (see Methods). For each scenario, the validation dataset shown in the plot is well-described by the corresponding prediction intervals. The worst case scenario V predicts an upper limit of 1,171 cycles that appear randomly in the phylogeny. The statistical noise in all scenarios is below the observed number of 2,899 cycles in the GISAID dataset.

The number of topological features is statistically significant. We estimated the expected number of topological cycles created by random homoplasic events by simulating several evolutionary scenarios under the following assumptions: uniform probability distribution for substitutions across the genome, no variations in fitness, and zero recombination rate. The simulations were performed with SANTA-SIM [19], implementing a Wright-Fisher model for evolutionary scenarios that realize different choices of population growth and substitution rate (see Methods). The statistical analysis of persistence barcodes of the simulated data shows that in the GISAID dataset with 161,024 distinct sequences, it is unlikely to find more than 1,171 one-dimensional topological cycles (95% prediction interval upper limit, scenario V; see Figure 3).

We conclude that a large part of the 2,899 topological cycles in the GISAID dataset must be due to increased mutation probabilities, selection effects, recombination events, or systematic sequencing errors.

Performance analysis and comparison with phylogeny-based methods. Standard phylogenetic methods for the detection of convergent evolution in genomic datasets are based on the prior reconstruction of a phylogenetic tree. The independent occurrence of a given mutation in different branches of the tree is then taken as an indicator of convergence. These methods are able to effectively find homoplasies even for highly genetically diversified isolates. However, current phylogenetic inference techniques have an unfavorable scaling with the number of sequences due to the rapid growth of the number of trees representing possible evolutionary histories. In addition, it has been observed that finding a single phylogeny that optimally captures the evolutionary history of SARS-CoV-2 is problematic because the number of sequences is large and at the same time their genetic diversity is low [28].

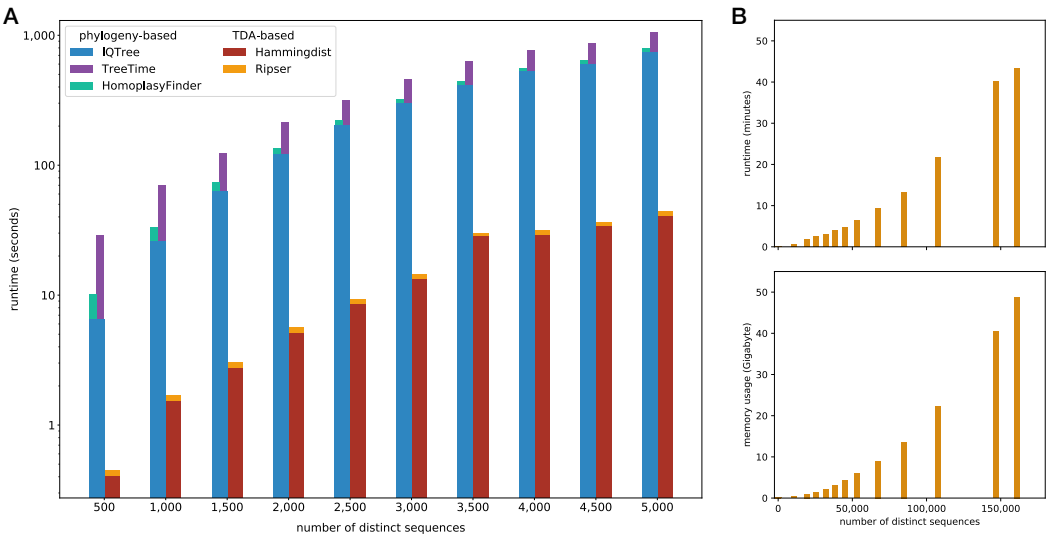

Figure 4. Performance analysis and comparison with phylogeny-based methods. (A) Basic runtime comparison between TDA-based methods and phylogeny-based methods for small random samples of SARS-CoV-2 genomes from the GISAID dataset. We used `IQTree` [27] to reconstruct phylogenetic trees (with default settings and fast search option). The subsequent homoplasy analysis was performed with `TreeTime` [34] and `HomoplasyFinder` [5] (with default settings). For the TDA-approach we used `Hammingdist` to generate genetic distance matrices and `Ripser` (with scaling parameter threshold 2) for the subsequent computation of persistence barcodes (see Methods). The comparison was carried out on an Intel Xeon E7-4870 processor. The favorable overall scaling of TDA-based methods allows for the effective analysis of the full GISAID dataset. (B) Runtime and memory usage for the computation of persistence barcodes for all monthly sub-alignments of the GISAID dataset with `Ripser` (with scaling parameter threshold 2; see Methods). The generation of the genetic distance matrix of the full alignment with `Hammingdist` took 31 hours and 338 Gigabytes of memory. The computations were carried out on an Intel Xeon Gold 6230R processor.

Persistent homology provides a new approach to this problem by detecting convergent evolution on small genetic distance scales purely in terms of topological cycles, without the need of constructing any phylogenetic trees. Inferring convergent evolution via persistent homology allows for an effective analysis of large datasets that scales favorably with the number of sequences. This is exemplified by a basic runtime comparison with typical phylogeny-based methods for small samples of SARS-CoV-2 genomic data, and enables a rapid analysis of the full GISAID dataset comprising 161,024 genetically distinct sequences (see Figure 4 and Methods). The short runtimes needed for the computation of persistent homology with `Ripser` are largely due to the fact that the topological recurrence analysis is restricted to topological cycles on small genetic distance scales (the SNV cycles). We emphasize that in contrast to phylogenetic-based methods, our method only resolves homoplasies on small genetic distance scales.

Topologically recurrent mutations in the whole genome alignment. In the absence of convergent evolution, mutations that appear in topological cycles are expected to be equally distributed across all segregating sites, so that a tRI ≥ 2 is already a statistically significant signal ($p < 0.05$; see Methods). The result of the tRI analysis for the whole genome alignment of the GISAID dataset with a total of 1,684 SNV cycles is shown in Figure 5, and a full list of mutations with tRI ≥ 2 is available in Table S2. Most of the mutations with strong tRI signal are known to be highly homoplasic and lead to stability issues in the construction of SARS-CoV-2 phylogenies [6, 28, 38, 39]. In this way, persistent

A

SNV	SAAV	gene	tRI	prevalence
G11083T[1,2]	L3606F	ORF1ab	141	5%
C21575T[1,2]	L5F	S	97	2%
C15324T[1,2]	synonymous	ORF1ab	38	3%
C3037T[1,2]	synonymous	ORF1ab	34	96%
A17615G	K1383R	ORF1ab	33	6%
C2453T	L730F	ORF1ab	31	2%
A10323G[1,2]	K3353R	ORF1ab	29	2%
A23403G[1,2]	D614G	S	29	96%
G25563T[1,2]	Q57H	ORF3a	28	26%
C27964T[2]	S24L	ORF8	27	10%

B

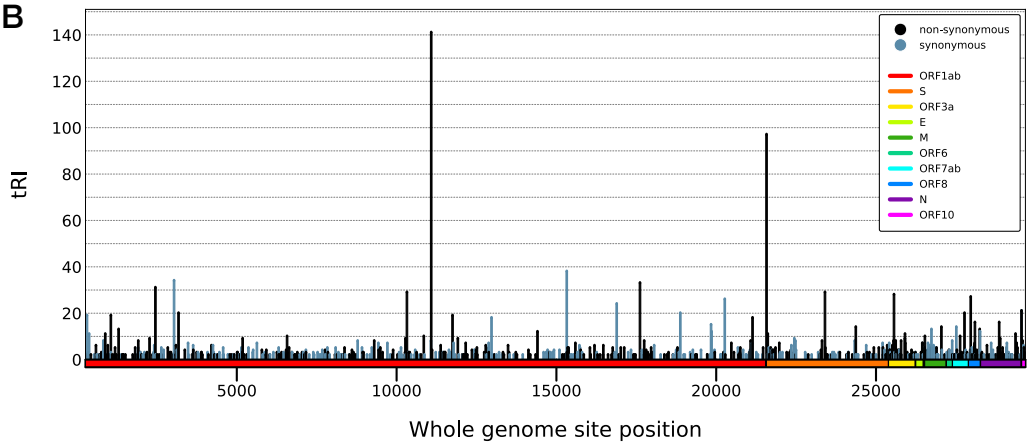

Figure 5. Topological signals of recurrent mutations across the whole genome. The table in (A) lists the topological recurrence index (tRI) and the prevalence of mutations with strongest topological signal. Many of these have previously been reported to be highly homoplasic in Turakhia *et al.*[1] [38] and van Dorp *et al.*[2] [39]. For a complete list of mutations with statistically significant topological signal (tRI ≥ 2) see Table S2. The histogram in (B) shows the distribution of topological signals across the whole SARS-CoV-2 genome. In every region of the genome, reticulate events play a crucial role in the evolution of the virus.

homology can aid the design of masking schemes in the phylogenetics of emerging pathogens. For example, `ORF1ab:G11083T` shows a steady increase in tRI over the whole course of the pandemic, while at the same time its prevalence remains low (Figure 6). A corresponding ancestral state reconstruction analysis based on the Nextstrain tree of a curated subsample of 3,507 sequences from the GISAID dataset as of 3 March 2021 [12], confirms that this mutation indeed arises repeatedly in independent and disjoint parts of the phylogeny, but was never established in larger subpopulations. Both synonymous and non-synonymous mutations with tRI ≥ 2 are spread across the whole genome, which reveals that the evolution of most parts of the genome violates the hypothesis of vertical evolution. The overall distribution of recurrent mutations across the genome is the result of many interfering biological processes, including recombination at several junction hotspots [10].

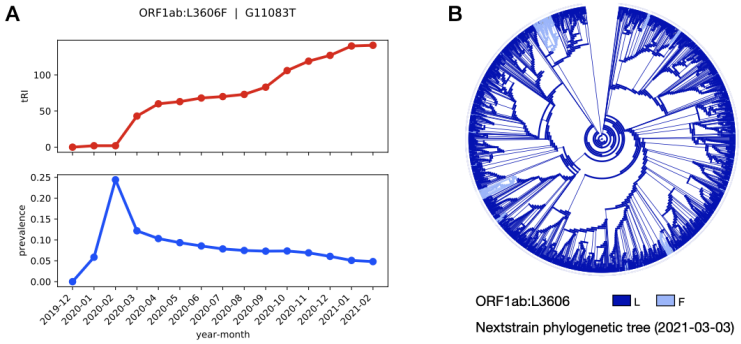

Figure 6. Topological footprint of a highly recurrent mutation in the example of the mutation `ORF1ab:G11083T`. (A) A time series analysis shows a monthly increase of the tRI, while the prevalence stays low. This indicates that the mutation has been re-emerging frequently and steadily since the beginning of the pandemic. The consistently low prevalence suggests that the mutation is neutral or deleterious, as a beneficial substitution would be expected to establish itself in larger subpopulations. In particular, this example shows that for certain mutations, tRI and prevalence are not correlated. (B) An ancestral state reconstruction analysis confirms the convergent evolution of `ORF1ab:G11083T` in terms of the repeated occurrence in independent branches of the Nextstrain tree [12] of a curated subsample of 3,507 sequences from the GISAID dataset as of 3 March 2021.

Identifying which mutations are topologically recurrent due to selective pressures requires additional information. For example, `S:D614G` was early on identified as a candidate for adaptation. There is now evidence that this mutation increases transmissibility [21, 23] and in vitro infectiousness [17, 33, 44]. So in this case, the prominent tRI signal of `S:D614G` in the whole genome alignment is likely a consequence of convergent evolution due to the increased fitness associated to the mutation. We find additional evidence of convergent evolution due to selective pressures by a more detailed analysis of the Spike gene.

Reticulate evolution of the Spike gene. While a persistent homology analysis of the whole genome data quantifies the reticulate evolution in SARS-CoV-2, which obstructs the construction of phylogenies for the whole genome, the chief public health interest lies in the evolution of the Spike protein. Of particular importance are the receptor-binding domain (RBD) and its vicinity, for which it is known from experiments that certain mutations enhance binding to the ACE2 receptor [35] or reduce binding of polyclonal convalescent plasma [9]. In order to probe the evolution of single genes for reticulate events, we run the persistent homology analysis for a suitable truncation of the alignment. In doing so for the Spike gene, we are able to investigate whether mutations arise recurrently also on this scale, which can be indicative of ongoing convergent evolution due to selective pressures. For the analysis of the Spike gene, a topological recurrence index tRI ≥ 8 is statistically significant ($p < 0.05$; see Methods). Results are shown in Figure 7 and a full list of Spike gene mutations showing some topological signal of recurrence is provided in Table S3. We find a large number of 10,814 topological cycles, including 10,677 SNV cycles, which implies that reticulate events have a significant impact

A

SNV	SAAV	tRI	prevalence
C22227T	A222V	776	19%
C21575T	L5F	466	2%
G22992A	S477N	433	4%
A23403G	D614G	400	96%
C21614T	L18F	362	8%
C21855T	S98F	342	2%
C22444T	synonymous	276	2%
G23593T	Q677H	251	1%
C23731T	synonymous	203	1%
C24334T	synonymous	193	4%
C22388T	synonymous	161	<1%
A22255T	synonymous	145	<1%
G25088T	V1176F	133	<1%
C21637T	synonymous	127	<1%
T24076C	synonymous	123	1%
C21846T	T95I	108	<1%

B

site position	total tRI per substitution
D936	Y:91, H:9, N:4, G:2, V:2, E:2
G75	V:43, R:12, S:4, D:2, A:2
G261	V:33, S:9, R:9, C:5, D:3
P26	S:46, L:34, H:8, T:3
D80	Y:60, N:10, A:8, G:3
H146	Y:22, Q:10, R:2, L:2
E156	D:5, Q:3, K:2, G:2
D215	H:41, Y:26, G:4, N:2
D427	Y:5, H:2, G:2, V:2
E484	K:49, G:10, Q:6, A:2
E554	D:6, Q:5, G:3, V:2
V622	F:44, I:8, L:3, A:3
P681	H:92, R:31, L:9, S:6
P1162	S:48, L:35, R:20, Q:3
D1199	Y:7, N:4, H:4, G:2
G1219	C:46, V:33, S:4, A:2

C

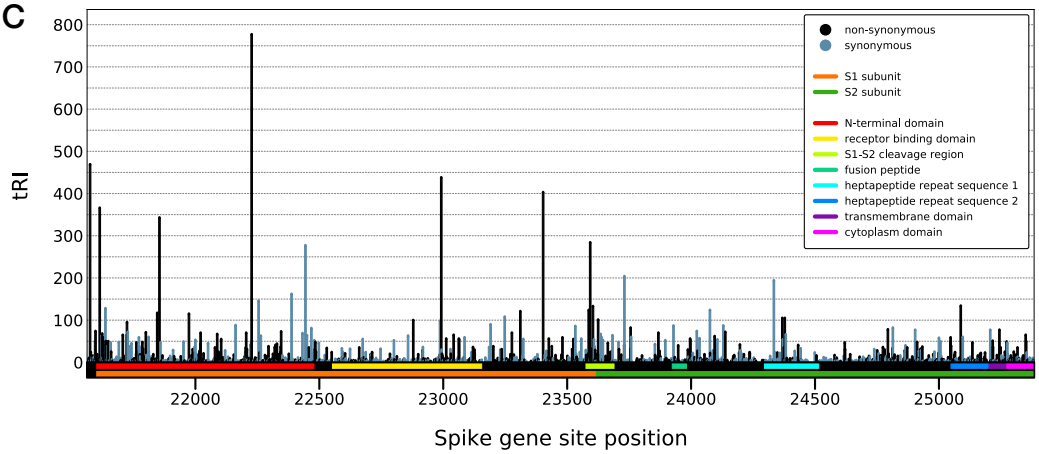

Figure 7. Topological signals of recurrent mutations across the Spike gene. (A) The table lists the topological recurrence index (tRI) and the prevalence of mutations with strongest topological signal. A mutation with tRI ≥ 8 is statistically significant. For a complete list of mutations showing any topological signal see Table S3. (B) Values of the tRI for highly variable amino acid site positions. For a complete list of all variable amino acid site positions see Table S4. (C) Histogram showing the distribution of topological signals across the Spike gene. There is an increase in topologically recurrent mutations in the S1 subunit and the S1-S2 cleavage region, as well as in the signal peptide at the beginning of the Spike gene.

on the evolution of the Spike protein in particular. From the distribution of topological signals for convergent evolution across the Spike gene (Figure 7), we notice a distinct accumulation for the S1 subunit, which is associated with host receptor recognition and contains epitopes for antibody binding [18]. Further visible hotspots include the Spike protein signal peptide, located at the very beginning of the gene, as well as the S1-S2-cleavage region, whose particular structure is suspected to be one reason for SARS-CoV-2 being more contagious than SARS-CoV [*op. cit.*]. A list of topologically salient mutations on the RBD is contained in Figure 9, and a comparison with known experimental results provides insights into the reasons for their recurrent behavior.

Features of mutations with strong topological footprint. Many of the Spike gene mutations that show topological signals for convergent evolution (Figure 7 and Figure 9) are known to have an adaptive effect on the virus either by increasing its fitness or by escaping the immune response of the host. The tRI analysis of the Spike gene highlights that the mutation `S:D614G` has in fact appeared independently several times, both before and during its increase in prevalence in early 2020. This is expected for a recurrent mutation that induces higher transmissibility [21, 23]. Moreover, the dynamics behind this behavior becomes visible from a time series analysis, which reveals a steady monthly increase in tRI until the new variant superseded the wild type in the population (Figure 8). The mutations `S:A222V` and `S:S477N` are associated with the lineage B.1.177 / 20E (EU1) which emerged in Europe

in mid-2020. While `S:S477N` is known to affect the binding affinity to the ACE2 receptor [35] leading to a slight increase in fitness, there is no conclusive evidence whether or not `S:A222V` also results in a higher transmissibility [15]. A particularly strong signal in our analysis that persists after the initial surge in prevalence in the European summer of 2020 suggests that `S:A222V` is notably recurrent, independently of its impact on viral fitness.

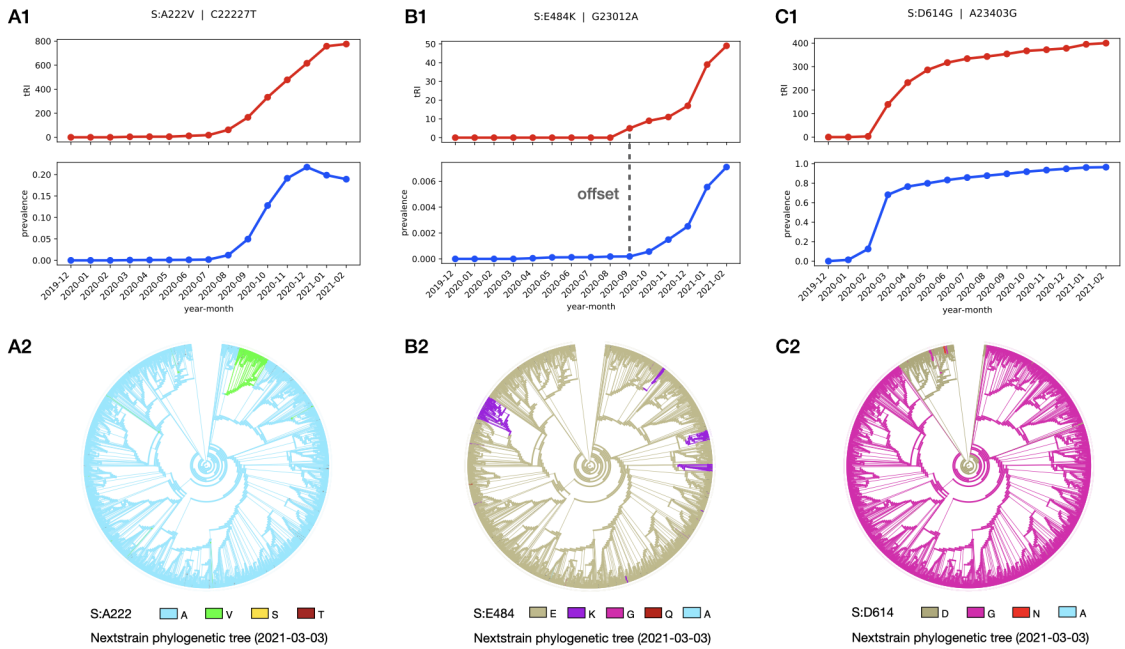

Figure 8. Typical time series and convergence patterns observed in the Spike mutations `S:A222V` (A), `S:E484K` (B) and `S:D614G` (C). The ancestral state reconstruction analysis is based on the Nextstrain tree of a curated subsample of 3,507 sequences from the GISAID dataset as of 3 March 2021 [12]. Recurrence of the mutation `S:A222V` persists after its initial surge in prevalence in mid-2020 (A1), but the mutation only got established in a subpopulation associated to the B.1.177 / 20E (EU1) lineage (A2). For `S:E484K`, the rise in tRI precedes the rise in prevalence with an offset of at least one month (B1). This serves as an early indicator for an immune escape mutation to establish itself in several subpopulations due to selective pressure (B2). For `S:D614G`, after a rapid increase in tRI and prevalence the tRI reaches a plateau (C1) once the mutation has become dominant, superseding the wild type in the early phase of the pandemic (C2).

We observe that on the RBD in particular, many of the topologically salient mutations appear in several variants of interest (VOI) or variants of concern (VOC) because of their phenotypic effects on the virus [42]. The substitutions `S:E484K`, `S:L452R`, `S:K417N` and `S:S494P` all result in a significantly reduced binding of polyclonal convalescent plasma and exhibit a distinct pattern in the times series analysis: a steady increase in tRI starting in late 2020, but before the eventual increase in prevalence (see Figure 8 and Figure S9). This pattern is compatible with the hypothesis that immune evasion manifests itself in convergent evolution in a host population with a rising level of immunity. Similarly, `S:N501Y` and `S:N501T` produce comparable signals in the tRI analysis and induce a slight antibody escape, which again is consistent with the corresponding time series analysis (Figure S9) and ancestral state reconstruction (Figure S10). The fact that `S:N501Y` has a comparatively high prevalence and is recognized in various VOI and VOC lineages is likely explained by the additional increase in ACE2 binding affinity for the asparagine-to-tyrosine substitution. A similar behavior is observed for `S:N439K` [37] and is likely the explanation for its strong topological signal.

Notably, the tRI values of the mutations `S:Y453F` and `S:F486L` exclusively originate from a small subpopulation closely related to the Cluster 5 mink variant [30, 41, 43]. The comparatively low values of the tRI suggest that both mutations have an adaptive effect in minks but do not significantly increase fitness of viruses circulating in the human population.

A

SAAV	tRI	tRI significant since	prevalence	notable lineages	ACE2-binding affinity[1]	mean plasma antibody escape[2]
S477N	433	2020-07	4%	B.1.160, B.1.526*	0.06	0.011
N439K	88	2020-04	2%		0.04	0.016
S494P	64	2020-09	<1%	B.1.1.7*	0	0.017
N501Y	55	2020-09	19%	B.1.1.7, P.1, B.1.351	0.24	0.011
N501T	50	2020-10	<1%		0.1	0.015
E484K	49	2020-09	<1%	B.1.1.7*, P.1, P.2, B.1.351, B.1.525, B.1.526*	0.06	0.066
A520S	35	2020-05	<1%		-0.04	0.0098
L452R	28	2020-12	1%	B.1.427, B.1.429, B.1.617	0.02	0.051
V367F	27	2020-03	<1%		0.07	0.015
A522S	27	2020-04	<1%		-0.03	0.0099
P384L	23	2020-04	<1%		0.01	0.022
A522V	21	2020-07	<1%		-0.03	0.010
F490S	19	2020-12	<1%		0	0.047
G446V	18	2020-10	<1%		-0.27	0.065
A475V	17	2020-04	<1%		-0.14	0.021
A348S	15	2020-10	<1%		0.01	0.011
V382L	14	2020-10	<1%		-0.05	0.012
P479S	14	2020-12	<1%		-0.03	0.0089
K417N	13	2021-02	<1%	P.1, B.1.351	-0.45	0.026
P384S	12	2020-12	<1%		-0.09	0.018
R408I	12	2020-11	<1%		-0.09	–
T478I	12	2020-12	<1%		-0.04	0.0082
Y508H	12	2020-07	<1%		0.07	0.017
S373L	11	2020-08	<1%		-0.02	0.011
E484G	10	2021-01	<1%		-0.06	0.065
A344S	9	2020-06	<1%		-0.14	0.0078
S477R	9	2021-02	<1%		-0.03	0.0089
N354D	8	2021-02	<1%		-0.04	0.024
Y453F	8	2020-06	<1%	Mink (Cluster 5)	0.25	0.015
S459F	8	2021-01	<1%		-0.1	0.0073
F486L	8	2020-05	<1%	Mink	-0.47	0.039
E516Q	8	2021-02	<1%		-0.05	–
T478K	7	–	<1%	B.1.617.2	0.02	0.0088
E484Q	6	–	<1%	B.1.617.1	0.03	0.062

B

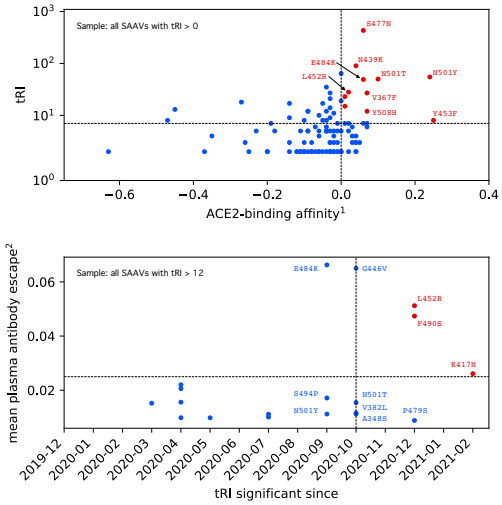

C

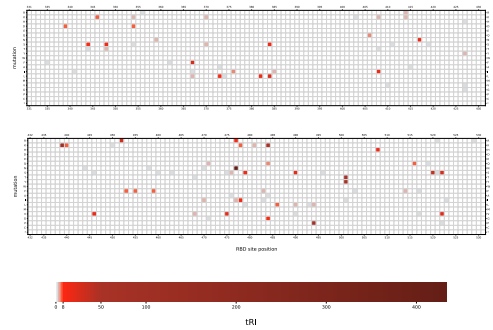

Figure 9. Topological signals of amino acid changes on the receptor-binding domain. The table in (A) shows all SAAVs with statistically significant topological recurrence index (tRI ≥ 8). For each mutation, its tRI together with the initial acquisition date of a significant tRI signal ($p < 0.05$) are shown. The table also provides prevalence, notable lineages containing the mutation ((*) indicates that this mutation is detected in some sequences but not all) [42], ACE2-binding affinity as in Starr *et al.*[1] [35], and mean plasma antibody escape as in Greaney *et al.*[2] [9]. (B) There is a strong correlation between significant tRI and an increase in ACE2-binding affinity (Fisher's exact test; $p < 0.01$), and we find that among highly topologically recurrent mutations the more recent ones are increasingly related with immune evasion (Fisher's exact test; $p < 0.05$). Panel (C) gives an overview of all amino acid variations across the receptor-binding domain showing topological signals of convergence. We find that the position `S:E484` is a particular hotspot for convergent evolution.

Topological recurrence correlates with adaptive phenotypes on the receptor-binding domain. Focusing the topological recurrence analysis for the Spike gene to the receptor-binding domain (see Figure 9 and Table S5), we can infer whether the topological recurrence index generally correlates with the phenotypic parameters associated with adaptation in [9, 35]. We observe a strong correlation between significant tRI ≥ 8 and an increase in ACE2-binding affinity compared to the wild type (Fisher's exact test, $p < 0.01$). We do not yet find a similar correlation between significant tRI and an increase in plasma antibody escape, which is in line with immune evasion only starting to gain relevance at the time of writing. Accordingly, among those mutations with strong topological signal of convergence (tRI > 12) we find a correlation between increased mean plasma antibody escape > 0.025 and

the initial acquisition of a significant tRI signal after October 2020 (Fisher's exact test, $p < 0.05$). A possible interpretation is a beginning shift towards immune escape as the driving force behind adaptation. Correspondingly, we expect immune evasion to cause increasingly strong topological signals in the ongoing pandemic when immunity is on the rise in the human population.

Early warning and surveillance of emerging adaptive mutations. As persistent homology is sufficiently sensitive to detect signals of convergent evolution already at very low mutation frequencies, we propose the topological recurrence index as an early warning system for emerging adaptive mutations. In particular, monitoring the tRI over time might aid vaccine development by the early identification of emerging vaccine resistance. Figure 9 features many mutations showing evidence of adaptation [9, 35] that have low prevalence so far, but give rise to notable signals of convergence in persistent homology. Among those are the mutations `S:L452R`, `S:T478K`, `S:E484Q` and `S:P681R` associated with the lineage B.1.617, which was linked with a major outbreak in India at the time of writing [4, 16]. The mutation `S:P681R` lies outside the receptor-binding domain, but yields a significant tRI signal in the Spike gene analysis (see Figure 7 and Table S3). The tRI signals for the mutations `S:T478K` and `S:E484Q` have not yet reached statistical significance, but show a rising tendency in February 2021 (see Figure S9). We further note that in a situation where sufficient genomic surveillance is available, the representation of reticulate events corresponding to adaptation in terms of SNV cycles provides geographic and temporal specifics which might be useful for public health decision making. Figure 10 depicts three examples of this application, with explicit cycles showing the acquisition of the mutation `S:E484K` in the variants of concern P.2 and B.1.1.7, and the emergence of `S:Y453F` in a subpopulation that is suspected to originate from mink populations [30, 41, 43].

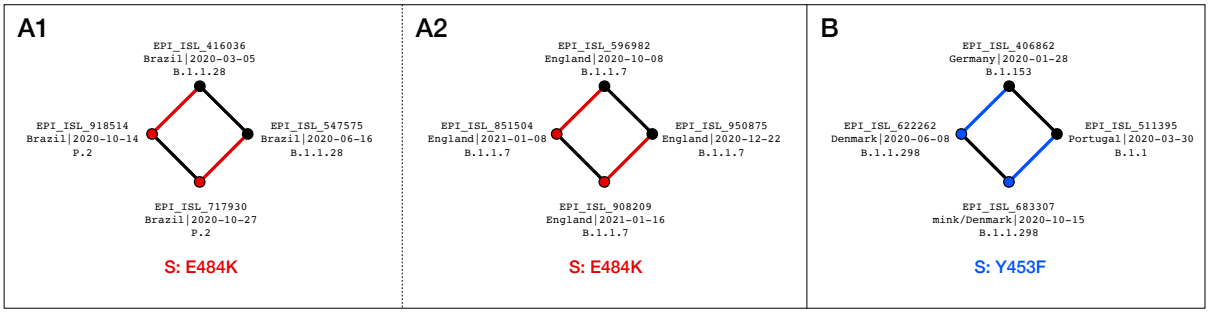

Figure 10. SNV cycles representing the acquisition of adaptive mutations in the evolution of the Spike gene. Panel (A) shows two instances of the mutation `S:E484K` arising independently, once in Brazil in October 2020 (A1), and once within the lineage B.1.1.7 in England in January 2021 (A2). Panel (B) shows the emergence of a variant containing the mutation `S:Y453F`, which is associated with adaptation to the mink host. One of the isolates was sampled from a mink, while the other one was taken from a patient in Denmark. Both are part of the lineage B.1.1.298 that is suspected to originate from mink populations [30, 41, 43].

Discussion

The identification of adaptive mutations in large genomic datasets is of paramount importance. In the current COVID-19 pandemic such mutations could be associated with vaccine resistance and higher transmissibility, among other concerning attributes. We present here a method that can rapidly identify the presence of these mutations.

Persistent homology provides an effective method to study convergent evolution of SARS-CoV-2 and is able to efficiently deal with the ever-increasing wealth of sequencing data created by global public

health surveillance. This novel tool rapidly extracts the associated global patterns from genomic data in an unbiased way and without relying on the prior reconstruction of a single phylogeny.

Applying this approach to an alignment of 303,651 viral genomes from GISAID representing the evolution of the pandemic from its beginning in late 2019 until February 2021, we found 2,899 instances of incompatible evolutionary histories, which are indicative of reticulate events such as homoplasies or recombinations shaping the evolution of the virus. By localizing these events on the genome, we found evidence for convergent evolution on several sites, some of which are already known to be highly homoplasic. A similar analysis for the Spike gene revealed a strong increase to 10,814 signals for reticulate events mostly located on the S1 subunit and the S1-S2 cleavage region, showing that convergence plays a significant role in the evolution of the Spike protein in particular. We observed that topologically salient mutations on the receptor-binding domain are generally linked with a change in phenotype associated with adaptation to the human host, and often convergently evolve in several variants of concern. We inferred that a leading selective pressure behind convergent evolution in the early phase of the pandemic is an increase in binding affinity to the ACE2 receptor, while immune escape is currently gaining importance in populations with rising levels of immunity. In particular, we found that persistent homology is sufficiently sensitive to detect these processes already at very low mutation frequencies, and is able to explicitly localize the acquisition of adaptive mutations in the dataset.

Based on these insights, we propose persistent homology as an early warning system for the emergence of new adaptive mutations in the ongoing SARS-CoV-2 pandemic and foresee this capability also in future pandemics of various pathogens. In addition, the early identification of variants of concern associated to adaptive mutations can guide experimentalists for the phenotypic characterization. We envision a combined effort between public health organizations with rapid sampling and sequencing of viral genomes, the computational characterization of potential adaptive variants and the experimental phenotypic characterization of these variants.

Methods

Data acquisition. We downloaded all SARS-CoV-2 genome sequences from the GISAID EpiCoV database as of 28 February 2021 (isolated from human and animal hosts) that carried the following attributes: "complete", "high coverage", "low coverage excluded", "collection date complete". This dataset comprised 450,473 sequences. A list of GISAID accession numbers of all sequences used in the present work, along with an acknowledgement of the contributions of both the submitting and the originating laboratories, is provided in Table S1.

Multiple sequence alignment. We aligned all sequences against the Wuhan/Hu-1 reference sequence `EPI_ISL_402125` in three stages: first, sequences were micro-aligned with two moving markers of 21nt

Figure 11. A schematic diagram of the Topological Data Analysis pipeline for the monitoring of emerging adaptive mutations in SARS-CoV-2.

length starting from the ends of the NCBI SARS-CoV-2 reference genome `NC_045512.2` (reference site positions 266 and 29,674). Subsequently all sequences containing ambiguous markers, or at least one ambiguous site (nucleotide "N") in between the markers, were removed. This resulted in a dataset comprising 304,714 sequences. Second, a subset of 128,347 sequences that deviated from the reference sequence in genome length, or whose genetic distance to the reference sequence was greater than 20nt, was aligned with `MUSCLE` [8], iteratively in blocks of 20 sequences each. Subsequently an alignment scheme for all sequences was derived. Third, all aligned sequences were truncated at reference site positions 266 and 29,674 to obtain complete SARS-CoV-2 genome sequences. All sequences still containing at least one ambiguous site (nucleotide "N") were removed. This resulted in an alignment comprising 303,651 sequences of length 30,130nt.

Time series, monthly sub-alignments, and distance matrices. We used `Hammingdist` [20] to compute the *genetic distance matrix* (Hamming distance) of the alignment of 303,651 whole genome sequences. Noteworthy, our convention in this work is that insertions and deletions (dashes in aligned sequences) do not contribute to the genetic distance.

We created 15 time buckets, each ranging from December 2019 to one of the months between December 2019 and February 2021. For each time bucket, a *time bucket sub-alignment* of all genetically distinct sequences whose collection dates belong to the given time bucket was created by selecting isolates by their date stamp and removing genetically identical sequences (Hamming distance = 0). The largest time bucket sub-alignment ranging from December 2019 to February 2021 contained 161,024 genetically distinct sequences. Then for each such sub-alignment the corresponding genetic distance matrix, which is a sub-matrix of the distance matrix of the whole alignment, was derived. We obtained 15 distance matrices of whole genome time bucket sub-alignments. This process was repeated for all sub-alignments after truncating sequences to the Spike gene (reference site positions 21,563 to 25,384). We obtained 15 distance matrices of Spike gene time bucket sub-alignments.

Topological Data Analysis and persistent homology. Topological Data Analysis is a field of data science that aims at extracting topological structures and patterns from datasets. Such topological structures have associated dimensions: structures of dimension 0 can be thought of as the connected components, and structures of dimension 1 are essentially the loops, or cycles, of the dataset. Structures of higher dimensions can also be defined, but are also more difficult to interpret. In this article, we are interested in reticulate evolutionary processes, thus we choose to focus on topological structures in dimension 1, since cycles can be interpreted as signals of divergence from phylogenetic trees.

Datasets often come as point clouds: in our setting, each point corresponds to a virus genome sample, and lies in a high-dimensional space where each nucleotide of the genome is a dimension. A common way to extract the phylogenetic network from this point cloud simply amounts to connecting samples as soon as their genetic distance is less than a given threshold $r > 0$. This results in a (neighborhood) graph, whose set of cycles provides candidates for the topological structures in dimension 1 of the true underlying network. Equivalently, this corresponds to put balls of radius r around each point, and to collect the loops formed by the union of balls. However, a main limitation of this approach comes from the fact that there might not exist a single correct r value (Figure 12).

The most common way to handle this issue in Topological Data Analysis is to actually compute and track the cycles for all possible values of r ranging from 0 to $+\infty$. As r increases, some cycles can appear, and some already existing cycles can disappear, or get filled in. The whole point of Topological Data Analysis is to record, for each cycle, its radius of appearance, or birth time, and radius of disappearance, or death time. This is called the *persistent homology* of the *Vietoris-Rips*

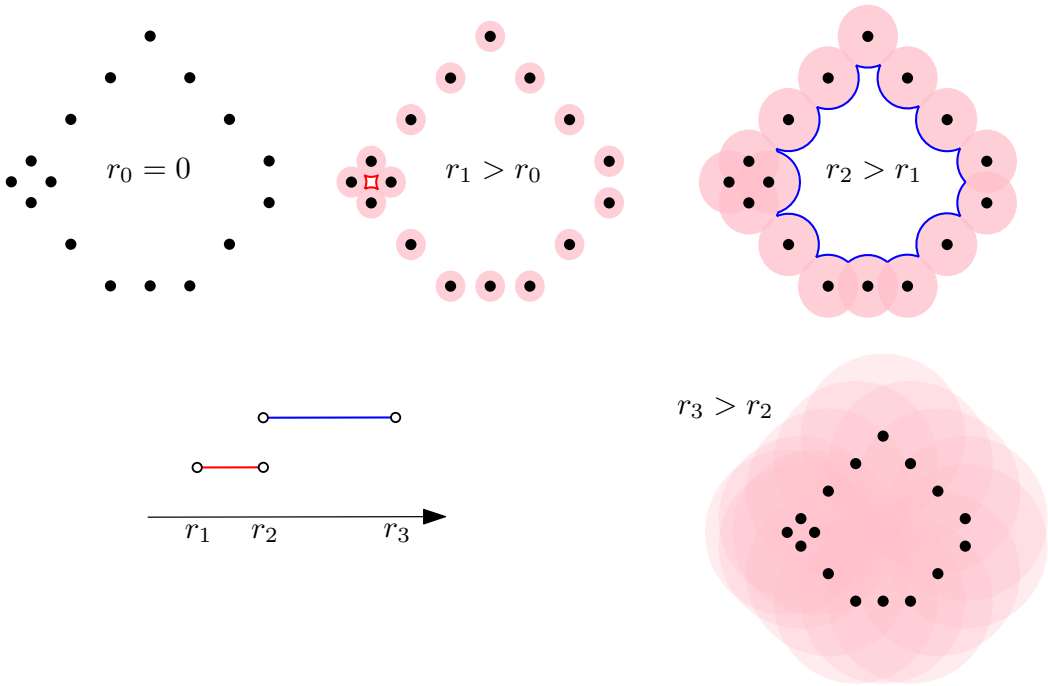

Figure 12. Illustration of the Vietoris-Rips filtration of a point cloud. Each point represents a sample, and we display the unions of balls of various radii $r_0 = 0 < r_1 < r_2 < r_3$. If one only chooses one radius, one might either see nothing (r_0, r_3), or detect the small red cycle but miss the large blue one (r_1), or vice-versa (r_2). A solution to handle this issue is to characterize each cycle with its radii of appearance and disappearance: the red cycle induces a red bar in the barcode with endpoints r_1 (for which the cycle is present in the union of balls) and r_2 (in which the cycle is filled in the union of balls), and similarly for the blue cycle.

filtration[2] corresponding to the point cloud. Hence, the Vietoris-Rips filtration provides a multiscale method to extract cycles of various sizes, and encode them in a so-called *persistence barcode*: each bar, or interval, in this barcode represents a cycle , i.e., in our case, a reticulate evolutionary process, and the bar endpoints correspond to its radii of birth and death, i.e., the maximum genetic distance between consecutive samples forming the cycle, and, roughly, the maximum pairwise genetic distance between samples forming the cycle. Moreover, the length of the bar represents the cycle size. In our case, this corresponds to the length of the reticulate evolutionary process, which allows to distinguish, for instance, between homoplasies and recombinations.

Computing persistent homology. A limitation of most of the algorithms in the literature that compute the persistent homology of Vietoris-Rips filtrations, is that they do not provide the samples forming the cycles corresponding to the bars in the barcode. Fortunately, this feature became recently available for the software `Ripser` [2], so we used it to compute the persistent homology of the Vietoris-Rips filtration associated to the genetic distance matrix for each time bucket sub-alignment (whole genome and Spike gene). As we are only interested in SNV cycles, the computation of persistence barcodes for the time bucket sub-alignments was restricted to small genetic distance scales (`Ripser` scaling parameter threshold set to 2), which greatly increases the speed of the computation.

[2]Formally speaking, this construction is actually called the *Čech filtration*. The Vietoris-Rips filtration is just a tractable approximation of the Čech filtration, which shares its essential properties.

`Ripser` is a state-of the art software for the computation of persistent homology based on the topological construction of Vietoris-Rips complexes. This construction, based on a scale parameter r, can be summarized as follows. The input is a distance matrix describing the dataset, considered as a finite metric space. First, consider the *geometric graph* at scale r, whose vertices are the data points, with any two points connected by an edge whenever their distance is at most r. Generalizing this construction, the *Vietoris-Rips complex* at scale r connects any subset of the data points with a simplex (an edge, a triangle, a tetrahedron, or a higher-dimensional generalization thereof) whenever all pairwise distances in the subset are at most r. A Vietoris-Rips complex is a particular type of *simplicial complex*, a higher-dimensional generalization of graphs which is of crucial interest in algebraic topology, in particular in homology theory.

For the computation of the persistence barcode, `Ripser` resorts to various optimizations, which are crucial when handling datasets of the size considered in the present work. Notably, `Ripser` computes persistent cohomology, which is not based on cycles but instead on cocycles, often described intuitively as *cuts* that tear open a hole. In order to obtain the requisite cycles representing the features in persistent homology, we used a custom version of `Ripser` that subsequently carries out a second computation, this time based on cycles instead of cocycles. While a naive computation based on homology would be prohibitively expensive, the previous computation of the persistence barcode based on cocycles makes the subsequent computation of representative cycles feasible.

The homological features identified by persistent homology admit different representative cycles. In order to obtain cycles that fit tightly to the data points, we use a method called *exhaustive reduction* [7, 46], which can be roughly summarized as follows. Whenever a representative cycle contains an edge that also appears in another cycle as the longest edge, a tighter representative can be obtained by replacing the edge with the remaining edges from the other cycles, which all have shorter length.

Topological recurrence analysis. For each time bucket sub-alignment (whole genome and Spike gene) a complete list of SNV cycles (one-dimensional cycles all of whose edges have genetic length 1nt) in this alignment was generated from the corresponding `Ripser` output. For each edge in an SNV cycle the endpoints of the edge correspond to a pair of uniquely determined sequences in the alignment that differ in exactly one nucleotide site position and hence determine an SNV. A list of all such edges that have the following two additional properties was compiled: (i) one of the two sequences associated with the endpoints shares a nucleotide with the reference sequence at the SNV site position, and (ii) the SNV is isolated in the sense that at the two preceding and following site positions the nucleotides are the same as in the reference sequence. Condition (ii) ensures that the corresponding SAAV is uniquely determined by the SNV for all edges carrying that SNV. Then for each SNV in that list, its *topological recurrence index* (tRI) is by definition the total number of all SNV cycles containing an edge that gives rise to the given SNV. We computed the tRI of each such SNV for every time bucket sub-alignment (whole genome and Spike gene). Moreover, for every whole genome time bucket sub-alignment the prevalence of every SNV was computed as the quotient of the number of all sequences carrying that SNV by the number of all sequences in that sub-alignment. Note that the sub-alignments entering into this computation consisted of genetically distinct sequences. Finally, for every SNV the measurements of both tRI (whole genome and Spike gene) and prevalence for all time buckets were combined into a time series analysis chart. Even if all 1,684 SNV cycles arose through random processes, it is expected that the resulting tRIs are distributed uniformly among all observed mutations. So the probability for a given mutation to have tRI$\geq k$ is given by a binomial distribution where the number of trials corresponds to the number of mutations in SNV cycles, and the probability for success is the inverse of the number of mutations that are realized in the dataset. From this we deduce that in the whole genome analysis tRI≥ 2 is highly significant ($p < 0.01$), while for the Spike gene analysis any value tRI ≥ 8 is significant ($p < 0.05$).

Ancestral state reconstruction analysis. For the study of the evolutionary histories of topologically highly recurrent mutations, we performed ancestral state reconstruction analyses using Mesquite Version 3.61 [26]. As inputs we used a curated alignment of 3,507 genome sequences and its corresponding Maximum-Likelihood tree, downloaded from Nextstrain [12] on 3 March 2021. The tree was rooted using the oldest sequence available (`EPI_ISL_406798`, collected on 26 December 2019). We inferred the evolution of each amino acid of interest along this SARS-CoV-2 tree using a parsimony approach.

Simulations. We checked the significance of persistent homology as an indicator of increased mutability or increased fitness by comparing the real dataset to simulations under the null-hypothesis of completely neutral evolution. The datasets were simulated with SANTA-SIM [19], which produces forward simulations of viral evolution based on a Wright-Fisher model. By completely neutral evolution we mean a Wright-Fisher model of viral evolution with uniform mutation probabilities for all substitions across the genome, no fitness variations among individuals and no recombination events. The parameters of the model are as follows.

- number of generations: $N = 10,000$
- number of sequences sampled from the population per time step: $n = 15$
- recombination rate: $\rho = 0$
- mutation rate per site per generation: μ
- effective initial population: p
- carrying capacity: c
- population growth rate per generation: g

In order to estimate the effect of these parameters on the number of expexted one-dimensional cycles in the GISAID dataset, we considered five scenarios. In scenarios I-III we varied the mutation rate under the assumption of fixed population size, while in scenarios IV and V we investigated the effects of logistic growth of the viral population. An overview of the parameters for each scenario is in Table 1.

The range of mutation rates in scenarios I-III were chosen such that the diversity in the simulated phylogenies are in close correspondence to the observed diversity in the GISAID dataset. While a mutation rate of $\mu = 0.75E-7$ substitutions per generation per site systematically underestimates the maximal distances to the root, the highest value of $\mu = 1.25E-7$ produces slightly larger maximal values (Figure S6). In fact, scenario II with $\mu = 1.00E-7$ reproduced the observed maximal distance accurately and provides a good approximation of the GISAID dataset. Major differences

scenario	mutation rate μ [10^{-7} subst./(site×gen.)]	growth rate g [1/gen.]	initial population p / carrying capacity c
I	0.75	0	$p = c =$ 100, 500, 1000, 2500, 5000, 7500, 10^4, 10^5, 10^6
II	1	0	
III	1.25	0	
IV	0.75	2	$p = 100$ / $c =$ 100, 500, 1000, 2500, 5000, 7500, 10^4, 10^5, 10^6
V	0.75	5	

Table 1. Parameters in scenarios I-V. Scenarios I-III vary over a range of mutation rates that roughly captures the diversity of the GISAID dataset. Scenarios IV and V probe the influence of logistic population growth. For all scenarios we produced 100 simulations for each of the values of the carrying population $c \leq 10^5$, and 5 simulations for $c = 10^6$.

scenario	I	II	III	IV	V
95% PI	[692, 814]	[362, 408]	[211, 237]	[646, 727]	[1023, 1171]

Table 2. 95% Prediction intervals for each scenario in datasets with 161,024 distinct sequences.

between simulations and the GISAID dataset in Figure S6 arise due to real-world effects like growth of population size, increase in worldwide sequencing rates, and enhanced spread of certain variants in the phylogeny.

In order to keep the overall runtime and memory usage at a reasonable level, we extrapolated results of the persistent homology analysis for smaller simulated datasets to the size of the GISAID dataset. For all scenarios we produced 100 simulations for each of the following values of the effective population p (resp. carrying capacity c): $100, 500, 1000, 2500, 5000, 7500, 10^4, 10^5$. Additionally, we included 5 simulations for $p = 10^6$ to achieve a better support of the extrapolation fit. For each value of p we randomly chose 60% of the simulations as training data, used to determine the parameters of different models in a non-linear least squares fit, while the remaining 40% were dedicated for later validation and comparison of the models.

For each scenario we considered a quadratic, cubic, powerlaw and exponential model for the observed points (x_i, y_i), and linear and powerlaw fits for the squared residuals $(y_i - y_{\text{fit}}(x_i))^2$ in the training data (Figure S8). In each model, we then used the resulting fits $\text{mean}(x)$ and $\text{var}(x)$ as estimators for the mean and variance of an underlying Panjer $(a, b, 0)$-class distribution [31, 36]. The quantiles of the observed number of cycles in the training data fit the quantiles of the Panjer distribution with corresponding mean and variance remarkably well, see Figure S7.

We then determined the likelihood $L = \prod_i P_{\text{Panjer}}(y = y_i | \text{mean}(x_i), \text{var}(x_i))$ to observe the validation data $\{(x_i, y_i)\}$. For each model, the corresponding log-likelihoods are listed alongside the corresponding fits in Figure S8. According to the log-likelihoods, the variance of the Panjer distribution is generally best described by a powerlaw behaviour. An exception is scenario II, for which the small sample of 5 simulations at $p = 10^6$ has an uncharacteristically small variance that skews the fits and corresponding likelihoods. Among the models that assume a powerlaw dependence of the variance, again with exception of scenario II, the cubic-powerlaw model yields maximum likelihoods.

Finally, we determined the 95% prediction intervals for the expected numbers of random cycles by use of the cubic-powerlaw extrapolation of mean and variance of a Panjer distribution (Table 2). Figure 3 shows the extrapolation of 95% prediction intervals for each scenario, together with the validation data. As an immediate observation, the validation data of scenarios I, IV and V, which were all based on the same mutation rate, are well described by the prediction intervals of scenario I. The prediction intervals of scenario V differ significantly from the other two only at high numbers of distinct sequences. This difference arises because simulations in scenario V generally produce less distinct sequences than scenario I and IV, such that a steeper extrapolation is not penalized sufficiently. Hence, the prediction intervals of scenario V illustrate the error margins of the extrapolations, but are not likely to faithfully represent the expected number of one-dimensional cycles. We also observe that higher mutation rates in scenarios II and III lead to smaller numbers of one-dimensional cycles in the dataset.

In conclusion, the 95% prediction interval of scenario V yields an upper bound of $[1023, 1171]$ expected random cycles in the GISAID dataset with 161,024 distinct sequences. Accordingly, the 2,899 one-dimensional cycles in the GISAID dataset cannot be explained by statistical noise. Moreover, since the diversity of the GISAID dataset is better approximated by scenario II than by scenarios I, IV or V, it is reasonable to rely on the prediction interval of scenario II, which predicts that in 95% of the cases we expect between $[362, 408]$ random cycles.

Acknowledgements

The authors acknowledge scientists and laboratories for sharing SARS-CoV-2 genome sequencing data with the research community via the GISAID database. A list of all contributions used in this work detailing authors from the originating laboratories responsible for obtaining the specimens and the submitting laboratories where genetic sequence data were generated is available in Table S1. This work was supported by the BMBF-funded de.NBI Cloud within the German Network for Bioinformatics Infrastructure (de.NBI) (031A532B, 031A533A, 031A533B, 031A534A, 031A535A, 031A537A, 031A537B, 031A537C, 031A537D, 031A538A). The authors acknowledge the use of de.NBI cloud and the support by the High Performance and Cloud Computing Group at the Zentrum für Datenverarbeitung of the University of Tübingen and the Federal Ministry of Education and Research (BMBF) through grant no 031 A535A. They thank M. Hanussek for IT support and early access to VALET [13]. The authors further acknowledge support from the Interdisciplinary Center for Scientific Computing at Heidelberg University and the development work of the Scientific Software Center of Heidelberg University carried out by D. Kempf and L. Keegan. This research was supported by the DFG Collaborative Research Center SFB/TRR 109 "Discretization in Geometry and Dynamics". M.B. was supported by the Deutsche Forschungsgemeinschaft (DFG, German Research Foundation) under Germany's Excellence Strategy EXC 2181/1 - 390900948 (the Heidelberg STRUCTURES Excellence Cluster). L.H. thanks the Evangelisches Studienwerk Villigst for their support. A.O. acknowledges funding by the Deutsche Forschungsgemeinschaft (DFG, German Research Foundation) – 281869850 (RTG 2229).

Author Contributions

M.B., L.H., A.O., J.P.G., R.R. designed the study; M.B., L.H., A.O. curated data; M.B., M.C., L.H., A.O., J.P.G. performed computational analyses; U.B., M.B., L.H., A.O. developed and implemented software; M.B., L.H., A.O. acquired computing resources; M.B., L.H., A.O. drafted the manuscript; all authors contributed to the final version of the paper.

Disclosure of Potential Conflicts of Interest

R.R. is a founder of Genotwin, he is member of the Scientific Advisory Board of AimedBio and consults for Arquimea Research.

References

1. Andersen, K. G., Rambaut, A., Lipkin, W. I., *et al.* The Proximal Origin of SARS-CoV-2. *Nature Medicine* **26,** 450–452 (2020). doi:10.1038/s41591-020-0820-9.
2. Bauer, U. Ripser: Efficient Computation of Vietoris-Rips Persistence Barcodes. *Journal of Applied and Computational Topology (to appear)* (2021). doi:10.1007/s41468-021-00071-5. arXiv: 1908.02518.
3. Chan, J. M., Carlsson, G. & Rabadan, R. Topology of Viral Evolution. *Proceedings of the National Academy of Sciences* **110,** 18566–18571 (2013). doi:10.1073/pnas.1313480110.
4. Cherian, S., Potdar, V., Jadhav, S., *et al.* Convergent Evolution of SARS-CoV-2 Spike Mutations, L452R, E484Q and P681R, in the Second Wave of COVID-19 in Maharashtra, India. *preprint* (2021). doi:10.1101/2021.04.22.440932.

5. Crispell, J., Balaz, D. & Gordon, S. V. HomoplasyFinder: A Simple Tool to Identify Homoplasies on a Phylogeny. *Microbial Genomics* **5** (2019). doi:10.1099/mgen.0.000245.

6. De Maio, N., Walker, C., Borges, R., *et al. Issues with SARS-CoV-2 Sequencing Data - SARS-CoV-2 Coronavirus / nCoV-2019 Genomic Epidemiology* Virological. https://virological.org/t/issues-with-sars-cov-2-sequencing-data/473.

7. Edelsbrunner, H. & Ölsböck, K. Holes and Dependences in an Ordered Complex. *Computer Aided Geometric Design* **73,** 1–15 (2019). doi:10.1016/j.cagd.2019.06.003.

8. Edgar, R. C. MUSCLE: Multiple Sequence Alignment with High Accuracy and High Throughput. *Nucleic Acids Research* **32,** 1792–1797 (2004). doi:10.1093/nar/gkh340.

9. Greaney, A. J., Loes, A. N., Crawford, K. H., *et al.* Comprehensive Mapping of Mutations in the SARS-CoV-2 Receptor-Binding Domain That Affect Recognition by Polyclonal Human Plasma Antibodies. *Cell Host & Microbe* **29,** 463–476.e6 (2021). doi:10.1016/j.chom.2021.02.003.

10. Gribble, J., Stevens, L. J., Agostini, M. L., *et al.* The Coronavirus Proofreading Exoribonuclease Mediates Extensive Viral Recombination. *PLOS Pathogens* **17,** e1009226 (2021). doi:10.1371/journal.ppat.1009226.

11. Gromov, M. in *Essays in Group Theory* (ed Gersten, S. M.) 75–263 (Springer, New York, NY, 1987). doi:10.1007/978-1-4613-9586-7_3.

12. Hadfield, J., Megill, C., Bell, S. M., *et al.* Nextstrain: Real-Time Tracking of Pathogen Evolution. *Bioinformatics* **34,** 4121–4123 (2018). doi:10.1093/bioinformatics/bty407.

13. Hanussek, M. *VALET* 2021. https://github.com/MaximilianHanussek/VALET visited on 2021-06-01.

14. Hodcroft, E. B., De Maio, N., Lanfear, R., *et al.* Want to Track Pandemic Variants Faster? Fix the Bioinformatics Bottleneck. *Nature* **591,** 30–33 (2021). doi:10.1038/d41586-021-00525-x.

15. Hodcroft, E. B., Zuber, M., Nadeau, S., *et al.* Spread of a SARS-CoV-2 Variant through Europe in the Summer of 2020. *Nature,* 1–9 (2021). doi:10.1038/s41586-021-03677-y.

16. Hoffmann, M., Hofmann-Winkler, H., Krüger, N., *et al.* SARS-CoV-2 Variant B.1.617 Is Resistant to Bamlanivimab and Evades Antibodies Induced by Infection and Vaccination. *preprint* (2021). doi:10.1101/2021.05.04.442663.

17. Hou, Y. J., Chiba, S., Halfmann, P., *et al.* SARS-CoV-2 D614G Variant Exhibits Efficient Replication Ex Vivo and Transmission in Vivo. *Science,* eabe8499 (2020). doi:10.1126/science.abe8499.

18. Huang, Y., Yang, C., Xu, X.-f., *et al.* Structural and Functional Properties of SARS-CoV-2 Spike Protein: Potential Antivirus Drug Development for COVID-19. *Acta Pharmacologica Sinica* **41,** 1141–1149 (2020). doi:10.1038/s41401-020-0485-4.

19. Jariani, A., Warth, C., Deforche, K., *et al.* SANTA-SIM: Simulating Viral Sequence Evolution Dynamics under Selection and Recombination. *Virus Evolution* **5** (2019). doi:10.1093/ve/vez003.

20. Keegan, L. & Kempf, D. *Hammingdist: A Fast Tool to Calculate Hamming Distances* version 0.8. 2020. https://pypi.org/project/hammingdist/ visited on 2021-06-01.

21. Korber, B., Fischer, W. M., Gnanakaran, S., *et al.* Tracking Changes in SARS-CoV-2 Spike: Evidence That D614G Increases Infectivity of the COVID-19 Virus. *Cell* **182,** 812–827.e19 (2020). doi:10.1016/j.cell.2020.06.043.

22. Latinne, A., Hu, B., Olival, K. J., *et al.* Origin and Cross-Species Transmission of Bat Coronaviruses in China. *Nature Communications* **11,** 4235 (2020). doi:10.1038/s41467-020-17687-3.

23. Li, Q., Wu, J., Nie, J., *et al.* The Impact of Mutations in SARS-CoV-2 Spike on Viral Infectivity and Antigenicity. *Cell* **182,** 1284–1294.e9 (2020). doi:10.1016/j.cell.2020.07.012.

24. Lythgoe, K. A., Hall, M., Ferretti, L., *et al.* Shared SARS-CoV-2 Diversity Suggests Localised Transmission of Minority Variants (2020). doi:10.1101/2020.05.28.118992.

25. Lythgoe, K. A., Hall, M., Ferretti, L., *et al.* Within-Host Genomics of SARS-CoV-2 (2020). doi:10.1101/2020.05.28.118992.

26. Maddison, W. P. & Maddison, D. *Mesquite: A Modular System for Evolutionary Analysis.* version Version 3.61. 2019. http://www.mesquiteproject.org visited on 2021-06-01.

27. Minh, B. Q., Schmidt, H. A., Chernomor, O., *et al.* IQ-TREE 2: New Models and Efficient Methods for Phylogenetic Inference in the Genomic Era. *Molecular Biology and Evolution* **37,** 1530–1534 (2020). doi:10.1093/molbev/msaa015.

28. Morel, B., Barbera, P., Czech, L., *et al.* Phylogenetic Analysis of SARS-CoV-2 Data Is Difficult. *Molecular Biology and Evolution* (ed Malik, H.) msaa314 (2020). doi:10.1093/molbev/msaa314.

29. *Origin of SARS-CoV-2* World Health Organization. https://www.who.int/publications/i/item/origin-of-sars-cov-2 visited on 2021-05-25.

30. Oude Munnink, B. B., Sikkema, R. S., Nieuwenhuijse, D. F., *et al.* Transmission of SARS-CoV-2 on Mink Farms between Humans and Mink and Back to Humans. *Science (New York, N.y.)* **371,** 172–177 (2021). doi:10.1126/science.abe5901.

31. Panjer, H. H. Recursive Evaluation of a Family of Compound Distributions. *ASTIN Bulletin* **12,** 22–26 (1981). doi:10.1017/S0515036100006796.

32. Patiño-Galindo, J. Á., Filip, I., AlQuraishi, M. & Rabadan, R. Recombination and Convergent Evolution Led to the Emergence of 2019 Wuhan Coronavirus. *preprint* (2020). doi:10.1101/2020.02.10.942748.

33. Plante, J. A., Liu, Y., Liu, J., *et al.* Spike Mutation D614G Alters SARS-CoV-2 Fitness. *Nature* **592,** 116–121 (2021). doi:10.1038/s41586-020-2895-3.

34. Sagulenko, P., Puller, V. & Neher, R. A. TreeTime: Maximum-Likelihood Phylodynamic Analysis. *Virus Evolution* **4** (2018). doi:10.1093/ve/vex042.

35. Starr, T. N., Greaney, A. J., Hilton, S. K., *et al.* Deep Mutational Scanning of SARS-CoV-2 Receptor Binding Domain Reveals Constraints on Folding and ACE2 Binding. *Cell* **182,** 1295–1310.e20 (2020). doi:10.1016/j.cell.2020.08.012.

36. Sundt, B. & Jewell, W. S. Further Results on Recursive Evaluation of Compound Distributions. *ASTIN Bulletin: The Journal of the IAA* **12,** 27–39 (1981). doi:10.1017/S0515036100006802.

37. Thomson, E. C., Rosen, L. E., Shepherd, J. G., *et al.* The Circulating SARS-CoV-2 Spike Variant N439K Maintains Fitness While Evading Antibody-Mediated Immunity. *preprint* (2020). doi:10.1101/2020.11.04.355842.

38. Turakhia, Y., De Maio, N., Thornlow, B., *et al.* Stability of SARS-CoV-2 Phylogenies. *PLOS Genetics* **16,** e1009175 (2020). doi:10.1371/journal.pgen.1009175.

39. Van Dorp, L., Acman, M., Richard, D., *et al.* Emergence of Genomic Diversity and Recurrent Mutations in SARS-CoV-2. *Infection, Genetics and Evolution* **83,** 104351 (2020). doi:10.1016/j.meegid.2020.104351.

40. Van Dorp, L., Richard, D., Tan, C. C. S., *et al.* No Evidence for Increased Transmissibility from Recurrent Mutations in SARS-CoV-2. *Nature Communications* **11,** 5986 (2020). doi:10.1038/s41467-020-19818-2.

41. Van Dorp, L., Tan, C. C., Lam, S. D., *et al.* Recurrent Mutations in SARS-CoV-2 Genomes Isolated from Mink Point to Rapid Host-Adaptation. *preprint* (2020). doi:10.1101/2020.11.16.384743.

42. *Variants of Interest and Variants of Concern.* Centers for Disease Control and Prevention. https://www.cdc.gov/coronavirus/2019-ncov/cases-updates/variant-surveillance/variant-info.html visited on 2021-04-14.

43. Welkers, M. R. A., Han, A. X., Reusken, C. B. E. M. & Eggink, D. Possible Host-Adaptation of SARS-CoV-2 Due to Improved ACE2 Receptor Binding in Mink. *Virus Evolution* (2020). doi:10.1093/ve/veaa094.

44. Yurkovetskiy, L., Wang, X., Pascal, K. E., *et al.* Structural and Functional Analysis of the D614G SARS-CoV-2 Spike Protein Variant. *Cell* **183,** 739–751.e8 (2020). doi:10.1016/j.cell.2020.09.032.

45. Zahradník, J., Marciano, S., Shemesh, M., *et al.* SARS-CoV-2 RBD *in Vitro* Evolution Follows Contagious Mutation Spread, yet Generates an Able Infection Inhibitor. *preprint* (2021). doi:10.1101/2021.01.06.425392.

46. Zomorodian, A. & Carlsson, G. Computing Persistent Homology. *Discrete & Computational Geometry* **33,** 249–274 (2005). doi:10.1007/s00454-004-1146-y.